Transition from steady to chaotic flow of natural convection on a section-triangular roof

Haoyu Zhai,[1,2,3] Juan F. Torres ⬤,[3] Yongling Zhao ⬤,[4] and Feng Xu ⬤[1,2,*]

[1]*School of Civil Engineering, Beijing Jiaotong University, Beijing 100044, China*

[2]*Beijing's Key Laboratory of Structural Wind Engineering and Urban Wind Environment, Beijing 100044, China*

[3]*Research School of Electrical, Energy and Materials Engineering, The Australian National University, Canberra ACT, Australia*

[4]*Department of Mechanical and Process Engineering, ETH Zürich, Zürich 8093, Switzerland*

Natural convection over a roof-shaped triangular surface is investigated using direct numerical simulations. The Rayleigh number (Ra) was varied from 1 to 5×10^6 with air as working fluid (Prandtl number of 0.71) at a fixed geometrical aspect ratio of 0.1, defined as the ratio of roof height to half-width. The transition route from a steady flow to a chaotic flow on the surface is characterized by the topological method with the increase of Ra. A weak flow, dominated by conduction, occurs when Ra was relatively small. As Ra increases, the convective flow becomes stronger and a sequence of bifurcations is found. Between Ra $= 10^2$ and 10^3, a primary pitchfork bifurcation occurs. Secondary and tertiary pitchfork bifurcations are observed in the range Ra $= [10^3, 10^4]$ and $[10^4, 10^5]$, respectively. After another pitchfork bifurcation at Ra $= [1.4, 1.5] \times 10^6$, which makes the plume tilt to either side of the roof top edge, a Hopf bifurcation is observed in Ra $= [1.9, 2] \times 10^6$, after which both the slope flow and plume become periodic. This is followed by further bifurcations including a period doubling bifurcation at Ra $\approx 3 \times 10^6$ and a quasiperiodic bifurcation firstly arising at Ra $\approx 3.4 \times 10^6$. Finally, the flow becomes chaotic for Ra $> 3.7 \times 10^6$. The state space, the maximum Lyapunov exponent, the fractal dimension, and the power spectral density are presented to analyze the flows in the transition to chaos. This work is a comprehensive description of the flow transition from steady state to chaos on surface of a section-triangular roof that is pertinent to various settings where fluid flow develops.

I. INTRODUCTION

Buoyancy driven flows over a flat surface have been a long lasting classic research topic of the fluid mechanics community [1–3]. One particular type of these flows is the one over an inclined plate, which has attracted much attention owing to its fundamental significance in both nature (mountain ridge and atmosphere pollution [4,5]) and industrial applications (building ventilation and solar energy [6–9]). The dynamics and heat transfer of this type of flows in various regimes, spanning from laminar to transitional and chaotic states, are of great scientific and engineering interest [10–12].

---

*Corresponding author: fxu@bjtu.edu.cn

When a fluid is heated by an inclined plate at a constant temperature, a thermal boundary layer forms and a subsequent slope flow driven by buoyancy rises along the plate. The flow on the surface of a section-triangular roof can be similarly divided into a buoyancy driven slope flow and a plume rising above the tip of the roof [13,14]. In early studies, Prandtl [15] first presented a theoretical solution under the Boussinesq approximation to investigate laminar natural convection on an inclined wall. Further research [16] used two-dimensional (2D) analysis to reveal heat transfer characteristics in laminar regime with varying angles of the heated plate, which is consistent with experiment results [17]. Based on those analysis, Fujii and Imura [18] investigated the heat transfer influenced by the Rayleigh number (Ra) and inclination angles in laminar, transitional, and turbulent regimes. The solution of Nusselt number scaled by $Ra^{1/5}$ or $Ra^{1/4}$ under different laminar regimes was established. However, although some of the flow structures were visualized, Fujii and Imura did not reveal a span-wise flow structure in detail. Vogt *et al.* [19] presented an interesting results about the transition from quasi2D flow to 3D flows and the occurrence of oscillations were observed. Dong *et al.* [20] proved that the flow fluctuation is influenced by the flow rotation. It reveals that complex dynamics exists inside the transition process.

It is well known that there are different flow regimes characterized by various structures, such as wavelike structures, which are influenced by the Rayleigh number (Ra) and the inclination angle [21], while the Nusselt number is proportional to $Ra^{1/5}$ in transitional and turbulence regimes. Scaling analysis have been widely used to investigate the dynamics and heat transfer of the flow on the inclined wall subject to different heating conditions [13,14,22–25]. It is concluded that the flow dynamics is mainly under four regimes: conduction-dominant, conduction-inertial, convection-inertial, and convection-viscous, which is determined by Ra, Prandtl number (Pr), and aspect ratio (A). Apart from the investigation in laminar regimes, many researchers paid attention to transition and turbulence regimes. An experiment in air was set up by Tritton [26] to study the development from transition to fully turbulent regimes with varying inclinations. However, the accuracy of results were largely influenced by the disturbance and method used in the experiment [27]. A further experiment was optimized by Al-Arabi and Sakr to examine the side effect on the flow over the inclined plate [28]. The following research by Sparrow and Husar [29] and Lloyd and Sparrow [30] visualized the instability in the span-wise direction and linked the beginning of transition to the first appearance of the longitudinal vortices. Detailed research by Black and Norries [31] focused the development of thermal waves inside the thermal boundary layer with the increase of local Ra number ($Ra^{1/3}$) and inclination angles ($\cos\theta$). Specific surface on the transition process was also concluded to have a crucial effect on transition [32]. Further, research [33–35] showed that the separation point and stability of the slope flow are also influenced by the inclination angle and Pr. Puigjaner *et al.* [36] used the Galerkin spectral method to simulate the bifurcation in a cubical enclosure heated from below. The critical Ra was found to be based on different flow patterns and dynamics. Torres *et al.* [37–39] then used a continuation method developed from a 3D spectral finite element code to produce comprehensive bifurcation diagrams of enclosed Rayleigh-Bénard (RB) convection in a tilted cavity under different Pr. They showed how multiple stable solution branches were influenced by the inclination angle.

After the separation of the slope flow above the top of the roof top edge, the plume rises [40]. Komori *et al.* [21] and Kimura *et al.* [41] visualized the plume that forms after the separation of the slope flow in transitional and turbulent regimes. Results showed that the formation of the plume enhances the heat transfer coefficient. The classic theory of the plume has been presented using ordinary differential equations to quantify entrainment [42]. Scaling analysis was used to investigate the relationship between dynamics or heat transfer and controlling parameters [13,14]. Much research has focused on the development of the plume in a closed volume [43,44] or under different heating sources or conditions [45–48]. Recently, the bifurcation of a plume was observed [49], demonstrating that the dynamics is different in two different scenarios (convection and conduction dominated) [50] and the different flow patterns that emerged are dependent on boundary conditions [51]. Furthermore, the transition in the plume from the laminar to the turbulent flow was found to associate with external disturbances [52–54], such as the periodic vortex-puffing

induced by intensive heating [55]. Qiao *et al.* [56,57] further investigated the plume rising from a vertical top-open cylinder heated from the cavity bottom. They reported a succession of bifurcations as Ra increases, giving a clear evolution of the route from laminar to chaos.

The literature review shows that little attention has been paid to the structure of the flow on a heated section-triangular surface that has a geometrical similarity with typical building roofs. Das and Basak [58] established numerical models having different symmetric structures with symmetric and asymmetric heating sources. However, they only focused on the flow structures with different heating sources and did not analyze the structure with increasing Ra under symmetric structure and heating sources. Kenjereš [59] investigated the heat transfer and flow structure in a symmetrically closed triangle cavity, concluding that the heat transfer coefficient for an inclined bottom becomes greater than that in a normal RB convection. Nonetheless, they did not investigate small inclination angles where interesting bifurcations and flow transitions are expected to occur. The range of Ra was also not very accurate and lacked detailed insight into the transitional regimes. Bhowmick *et al.* [60] first mapped a clear route from laminar to chaos in a 2D V-shaped cavity, but the development of flow structures in the span-wise direction could not be further investigated in 3D cavity. Gaby *et al.* [61] investigated the regime from transition to chaos of acoustically driven flow in a cavity and determined chaotic stages by Lyapunov exponent and phase space. Torres *et al.* [37] showed that the flow structure after the primary bifurcation in an RB cell differs between 2D and 3D cavities, the former yields a longitudinal roll [62] whereas the latter yields transverse rolls. Phase-shifting interferometer (PSI) and particle image velocimetry (PIV) techniques were used in further experiment investigation to visualize the flow structure [63].

As suggested by the above literature review, the bifurcation route for the near field flow on a slightly inclined roof has not been well understood. Only some preliminary 2D numerical investigations were sought by Zhai *et al.* [13,14] to validate the scaling analysis under conditions with a constant heating or a periodic heat flux. This motivates our further investigation using 3D models for flows on the surface of a section-triangular roof which is a common structure used in civil engineering for better water drainage and also energy savings in some cases. Based on Ref. [41], the flow structure could have both ascending and descending flow when the range of aspect ratio is between 0.1 and 0.26, enhancing the dynamics and heat transfer on the inclined plate. Similar results were also observed in Refs. [13,14]. The aspect ratio under the consideration of this work is therefore chosen to be at 0.1 to deepen understanding of this type of flow.

The main objective of this study is to investigate the transition from laminar flow to chaos of natural convection developed on the surface of a section-triangular roof. For the numerical method, direct numerical simulation (DNS) was proven as a proper method to investigate the transition inside thermal boundary layer [64,65]. Therefore, DNS are used in conjunction with a topological analysis. Different types of flow bifurcations are determined with the increment of Ra, and corresponding flow structures are characterized. Finally, the dynamics and heat transfer within different regimes during the course of transition are quantified.

II. MATHEMATICAL FORMULATION

A. Governing equations and controlling parameters

Natural convection from the surface of a section-triangular roof is governed by the normalized Navier-Stokes equations, i.e., the incompressible continuity equation, momentum equation with the Boussinesq approximation and energy equation:

$$\frac{\partial U}{\partial X} + \frac{\partial V}{\partial Y} + \frac{\partial W}{\partial Z} = 0, \tag{1}$$

$$\frac{\partial U}{\partial \tau} + U\frac{\partial U}{\partial X} + V\frac{\partial U}{\partial Y} + W\frac{\partial U}{\partial Z} = -\frac{\partial P}{\partial X} + \frac{\text{Pr}}{\text{Ra}^{1/2}}\left(\frac{\partial^2 U}{\partial X^2} + \frac{\partial^2 U}{\partial Y^2} + \frac{\partial^2 U}{\partial Z^2}\right), \tag{2.1}$$

$$\frac{\partial V}{\partial \tau} + U\frac{\partial V}{\partial X} + V\frac{\partial V}{\partial Y} + W\frac{\partial V}{\partial Z} = -\frac{\partial P}{\partial Y} + \frac{\mathrm{Pr}}{\mathrm{Ra}^{1/2}}\left(\frac{\partial^2 V}{\partial X^2} + \frac{\partial^2 V}{\partial Y^2} + \frac{\partial^2 V}{\partial Z^2}\right) + \mathrm{Pr}\,\theta, \tag{2.2}$$

$$\frac{\partial W}{\partial \tau} + U\frac{\partial W}{\partial X} + V\frac{\partial W}{\partial Y} + W\frac{\partial W}{\partial Z} = -\frac{\partial P}{\partial Z} + \frac{\mathrm{Pr}}{\mathrm{Ra}^{1/2}}\left(\frac{\partial^2 W}{\partial X^2} + \frac{\partial^2 W}{\partial Y^2} + \frac{\partial^2 W}{\partial Z^2}\right), \tag{2.3}$$

$$\frac{\partial \theta}{\partial \tau} + U\frac{\partial \theta}{\partial X} + V\frac{\partial \theta}{\partial Y} + W\frac{\partial \theta}{\partial Z} = \frac{1}{\mathrm{Ra}^{1/2}}\left(\frac{\partial^2 \theta}{\partial X^2} + \frac{\partial^2 \theta}{\partial Y^2} + \frac{\partial^2 \theta}{\partial Z^2}\right). \tag{3}$$

It has been known that the normalization equations are determined by the nondimensional parameters: Pr number and Ra number [24,66], which are defined as follows:

$$\mathrm{Ra} = \frac{g\beta\Delta T l^3}{\nu\kappa}, \tag{4}$$

$$\mathrm{Pr} = \frac{\nu}{\kappa}, \tag{5}$$

where g is the acceleration of gravity, β is the thermal expansion coefficient, ΔT is the temperature difference between heat plate T_{wall} and ambient fluid T_0, ν is the kinematic viscosity, κ is the thermal diffusivity, and l is the characteristic length, which is regarded as the half width of the triangular surface. The working fluid is air ($\mathrm{Pr} = 0.71$) while the buoyant conditions are set by varying Ra.

Additionally, previous studies [13,14] showed that natural convection on the inclined wall is also governed by the aspect ratio of the surface of a section-triangular roof, which is defined as

$$A = \frac{h}{l}, \tag{6}$$

where h is the height of the roof, i.e., the vertical component of the geometry.

The independent (space and time) and dependent (velocity, pressure, temperature) variables in Eqs. (1)–(3) were normalized as follows:

$$X = \frac{x}{l}, \quad Y = \frac{y}{l}, \quad Z = \frac{z}{l}, \tag{7.1}$$

$$U = \frac{u}{\kappa\mathrm{Ra}^{1/2}/l}, \quad V = \frac{v}{\kappa\mathrm{Ra}^{1/2}/l}, \quad W = \frac{w}{\kappa\mathrm{Ra}^{1/2}/l}, \tag{7.2}$$

$$\theta = \frac{T - T_0}{T_{\mathrm{wall}} - T_0}, \tag{7.3}$$

$$P = \frac{p}{\rho u^2}, \tag{7.4}$$

$$\tau = \frac{t}{l^2/\kappa\mathrm{Ra}^{1/2}}. \tag{7.5}$$

B. Direct numerical simulation

The potentially transient flow along the slope and in the rising plume from the surface of a section-triangular roof is investigated by DNS in static wind conditions using ANSYS Fluent 18.0. The governing equations are solved using the finite volume method with the SIMPLE algorithm [67]. The advection term is discretized by the QUICK scheme [68], and the transient term by the second-order difference (details could be seen in ANSYS Fluent 12.0 theory guide [69]). This numerical procedure has been successfully applied in much research using nondimensional governing equations [13,60,70]. The time step is determined by setting the Courant number in the range between 0.25 and 0.3 to guarantee the stability of the solution.
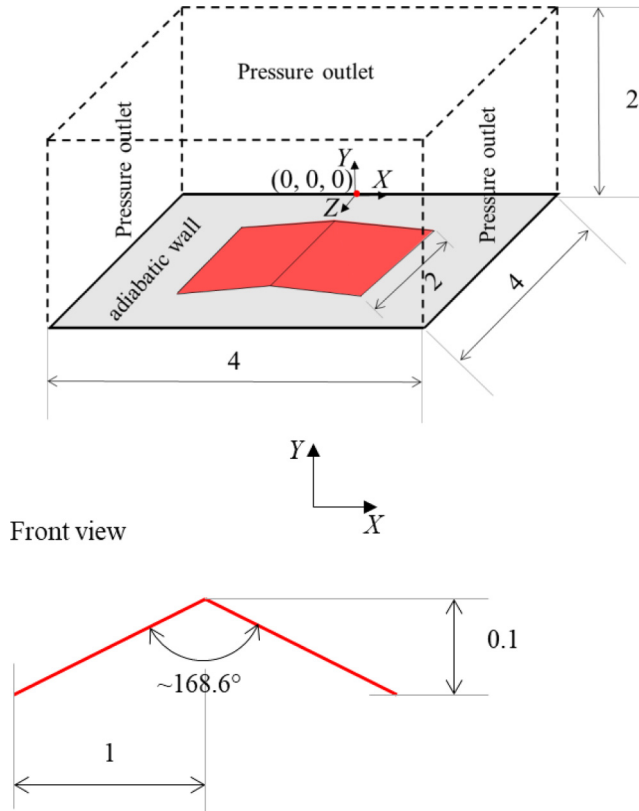
FIG. 1. Schematic of the computational domain and boundary conditions of natural convection around a section-triangular roof model. The surface on the bottom in red is isothermal, whereas the shadow surface is adiabatic.

A nonuniform grid is established using ANSYS/ICEM. Finer grids are applied at the proximity of the open boundaries and zones near the heated surface to guarantee that enough grid points are contained within the boundary near the rigid walls, as well as to not exceed the maximum Courant number in the vicinity of the open boundaries.

C. Geometry and boundary conditions

The transitional flow above the surface of section-triangular roof is taken into consideration. The schematic of the model is shown in Fig. 1. The spatial Cartesian coordinates X, Y, and Z represent the transverse, streamwise, and spanwise direction, and the origin is at the middle of the junction of the back and bottom planes. The nondimensional length, width, and height of the domain are $4 \times 4 \times 2$. The surface of section-triangular roof is extruded from a square base of each side 2, so that the aspect ratio of the surface becomes 0.1, i.e., forming an angle of $\sim 5.7°$ between the horizontal plane and a side of the surface, as shown in Fig. 1. The characteristic length is set to $l = 1$, while the aspect ratio is fixed to 0.1 to form a slight inclination that allows the creation of various flow bifurcations. To reduce the influence of the reverse flow through the boundary layer above the surface of section-triangular roof, the length and width of the domain are set to have a sufficiently large size by adding l in each direction. To investigate the plume after separation from the slope flow and prevent numerical deviation from the turbulent flow in the far field, the length in

TABLE I. Average temperature θ_{ave} on a line starting at point (0.5, 0.07, 1) and ending at point (0.5, 0.07, 3) for Ra $= 5 \times 10^6$ calculated using different domain size, approximately keeping the same mesh density.

No.	Domain size (numbers)	Time step	θ_{ave}	Variation (%)
1	$4 \times 4 \times 2$ (1M)	0.03	0.65178	–
2	$6 \times 6 \times 3$ (3.375M)	0.03	0.64841	-0.5

the y direction of the computing domain is set up to a value of $2\,l$. The surface of section-triangular roof is located at the center of the bottom of the computational domain.

The initial and boundary conditions of the governing equations Eqs. (1)–(3) are as follows:

(a) The dimensionless velocity and temperature in the entire domain, as well as in the initial boundary conditions, are set to zero.

(b) The bottom boundary is a rigid and no-slip wall where all velocity components are set to zero. The temperature of the surface of section-triangular roof is set to $\theta_{\text{wall}} = 1$ (Dirichlet boundary condition) throughout the simulation, so Ra was changed by modifying g in Eq. (4). The rest of the bottom boundary is adiabatic. It is worth noting that, in the numerical simulation, buoyancy in the fluid is produced by the isothermally heated inclined roof. That is, the temperature of $\theta_{\text{wall}} = 1$ is imposed on the inclined plate when $\tau > 0$, and thus an initially isothermal fluid is heated over time by the inclined plate, similar with the experiment (see Wang [71]) in which the time required for the plate to reach a specified temperature is much shorter than the time taken by the flow to fully develop.

(c) The open boundaries are set as a pressure-outlet boundary condition with zero velocity gradient (Neumann boundary condition) to minimize the influence of the boundary on the flow, i.e., $\partial U/\partial n = \partial V/\partial n = \partial W/\partial n = 0$, where n is the Cartesian coordinate normal to the boundary. The inflow temperature is set to the ambient temperature $\theta_{\text{fluid}} = 0$, whereas the outflow temperature at a boundary grid is set to that of the adjacent internal grid, i.e., Neumann boundary condition.

D. Verification and Validation

The domain size of $6 \times 6 \times 3$ was used to test the influence of the length scale in each direction. As listed in Table I, the average temperatures for Ra $= 5 \times 10^6$ (the largest value investigated in this study) along a line starting at point (0.5, 0.07, 1) and ending at point (0.5, 0.07, 3) were compared as a basis for the domain-independence study.

Time step and mesh independence tests were conducted with hexahedral (structured) meshes, the number of which are approximately 0.5 M, 1 M, 1.5 M, and 2 M, and the six nondimensional time steps from 0.015 to 0.12 were tested. The mesh was constructed with $\Delta X = 0.007$ adjacent to the center of the heated wall with an expansion a factor of 1.08 in the transverse direction (X), with $\Delta Y = 0.0032$ adjacent to the heated wall with an expansion factor of 1.03 in the streamwise direction (Y) and with a uniform grid distribution in the spanwise direction (Z). To test the mesh independence for different mesh grids and time steps, average temperatures along a line (same as Table I) are given in Table II for Ra $= 5 \times 10^6$. Based on the results in Table II, the mesh grid of $120 \times 72 \times 120$ was adopted because its deviation from the finest mesh is less than 3%, and the time step of 0.03 was selected for the same reason. Additionally, the typical nondimensional Kolmogorov length scale was also calculated to confirm that it satisfies the numerical requirements for DNS of chaotic flows in the investigated range of Ra. Detailed definition about Kolmogorov length scale may be found in Ref. [72]. In this study, the nondimensional Kolmogorov length scale in the thermal boundary layer is scaled as

$$\lambda_K = \frac{(2\pi)^{1/4}}{\text{Ra}^{3/8}\text{Pr}^{3/8}}. \tag{8}$$

TABLE II. Average temperature θ_{ave} on a line (same as Table I) for Ra $= 5 \times 10^6$ calculated using different grid point numbers and time steps.

No.	Mesh grid (numbers)	Time step	θ_{ave}	Variation (%)
1	$96 \times 57 \times 96$ (0.5M)	0.03	0.64394	-1.2
2	$120 \times 72 \times 120$ (1M)	0.015	0.65267	0.13
3	$120 \times 72 \times 120$ (1M)	0.03	0.65178	–
4	$120 \times 72 \times 120$ (1M)	0.06	0.64465	-1.1
5	$120 \times 72 \times 120$ (1M)	0.12	0.6462	-0.9
6	$136 \times 82 \times 136$ (1.5M)	0.03	0.66554	2.1
7	$150 \times 90 \times 150$ (2M)	0.03	0.66422	1.9

That is, the nondimensional mesh size near the heating boundary should be smaller than $\lambda_K = 0.0055$. Considering $\Delta Y = 0.0032$ which expanded by a factor of 1.03 in the streamwise direction (Y), it is clear that the first 20 mesh grids near the heating boundary are smaller than λ_K. This ensures the solution accuracy for the thermal boundary layer.

The experiment [41] performed for an inclined wall in an open water tank was used to validate the present numerical model, in which the inclined wall was heated with $q = 5000\,\mathrm{W\,m^{-2}}$ at Ra $= 10^7$ to 10^{11}. The good agreement of the local heat transfer coefficient between the experimental [41] and our numerical simulation results, as shown in Fig. 2, serves as the validation of our numerical model.

III. RESULTS AND DISCUSSION

To investigate the flow structures and dynamics in the transition from steady-state flow to chaos, numerical simulations were conducted in the range of Ra from 1 to 5×10^6, whose typical cases are also listed in Table III, together with representative simulation results discussed below. For the nondimensional governing equations, we could directly increase Ra. For ANSYS Fluent, the software used in this study, we increase Ra by changing g. The analysis is conducted while increasing Ra, starting with the conduction-dominant weak flow (Sec. III A), followed by the steady laminar flow after primary, secondary and tertiary pitchfork bifurcations (Sec. III B), further pitchfork bifurcations within the steady state regime (Sec. III C), transition to periodic (Sec. III D–Sec. III E) and quasiperiodic flows (Sec. III F), and finalizing in the route to chaos (Sec. III G).
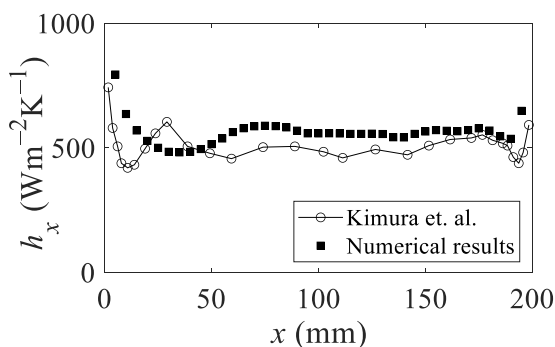

FIG. 2. Validation of the present numerical model based on the local heat transfer coefficient of a plate. The experimental result was from Kimura et al.. [41] for a slightly inclined, heated plate.

TABLE III. Rayleigh numbers and representative simulation results U_{Plume} for a working fluid of air ($\text{Pr} = 0.71$).

No.	Ra	U_{Plume}
1	10^0	5×10^{-8}
2	10^1	3.78×10^{-8}
3	10^2	2×10^{-9}
4	10^3	7×10^{-10}
5	10^4	4×10^{-8}
6	10^5	2.35×10^{-8}
7	$10^6 - 5 \times 10^6$	3×10^{-7} (Ra $= 10^6$), 2.79×10^{-6} (Ra $= 1.5 \times 10^6$)

A. Conduction-dominant weak flow for Ra $< 10^3$

In the range of relatively small Ra, from Ra $= 1$ to 10, when the surface of the section-triangular roof is heated by imposing a constant wall temperature, the heat transfer is dominated by conduction with a weak steady and 3D flow structure as shown in Fig. 3. As depicted in Figs. 3(a.1–3) and 3(b.1–3), there is no distinct thermal boundary layer or plume. A weak flow rises along the inclined wall with a stronger flow along the central axis, with symmetry planes on both $X = 0$ and $Z = 2$. With increase of Ra to 10^2, buoyancy becomes stronger and a slightly more distinctive plume starts to emerge downstream, as shown in Figs. 3(c. 1–3). Figures 3(a–c. 4) plot the temperature contours on the horizontal plane $Y = 1$ for three different Ra, which means that the near-field flow on the top of the surface is also symmetric with respect to the planes $X = 0$ and $Z = 2$ The high-temperature region is gradually becoming smaller with the increase of Ra from 10 to 10^2 based on Figs. 3(a–b. 4), and thus the plume is becoming thinner because of the stronger flow. It is worth noting that the flow still remains steady and symmetric with respect to both $X = 0$ and $Z = 2$ planes and only one pair of velocity roll exists in each direction.

B. Primary, secondary and tertiary pitchfork bifurcations and symmetry properties

As depicted in Figs. 4(a.1–3) and 4(b.1–3), with the increase of Ra from 10^3 to 10^4, a distinct thermal boundary layer occurs on the inclined wall and a single plume emerges from the top of the roof. Ridges (type of Ridge I) rising from four corners of the roof occur and become more distinct with the increase of Ra, as shown in Figs. 4(a–b. 1). The separation point between the slope flow and the plume moves towards the central vertical axis, as shown in Figs. 4(a–b. 2) and at the position of the red solid circle in Figs. 4(a–b. 3). Additionally, the plume stem attenuates and the velocity increases with the increase of Ra. The flow structure still remains symmetric with respect to the planes $X = 0$ and $Z = 2$. However, as illustrated by two brown solid circles in Figs. 4(c–d. 3), the plume stem is initially divided into two parts resulting from the leading-edge effect. Corresponding to the separation of the plume, the convective rolls also divide into two pairs which means that a transition of the flow pattern may occur in this range.

When further increasing Ra to 10^5, the stem of the plume appears to have an even more distinctive structure. The separation between the slope flow and plume occurs near the roof top edge. The flow structure still appears to be 2D symmetric with respect to both $X = 0$ and $Z = 2$ planes as shown in Fig. 4(c). However, as shown in Figs. 4(c–d. 1) and 4(c–d. 3), the combined plume stem separates into two individual parts in Z direction with respect to $Z = 2$ plane together with the development of four ridges (type of Ridge II) rising from the four corners when Ra reaches 10^6. Furthermore, convection dominates the flow as evidenced by the appearance of a plume cap in Fig. 4(d. 2).

To understand further bifurcation in the transition, the topological method [73] is used. The application of the topological result to the fluid flow is to convert the flow domain into an n-fold torus (Metcalfe and Ottino [74]). Here, some part of streamlines in the X direction can be
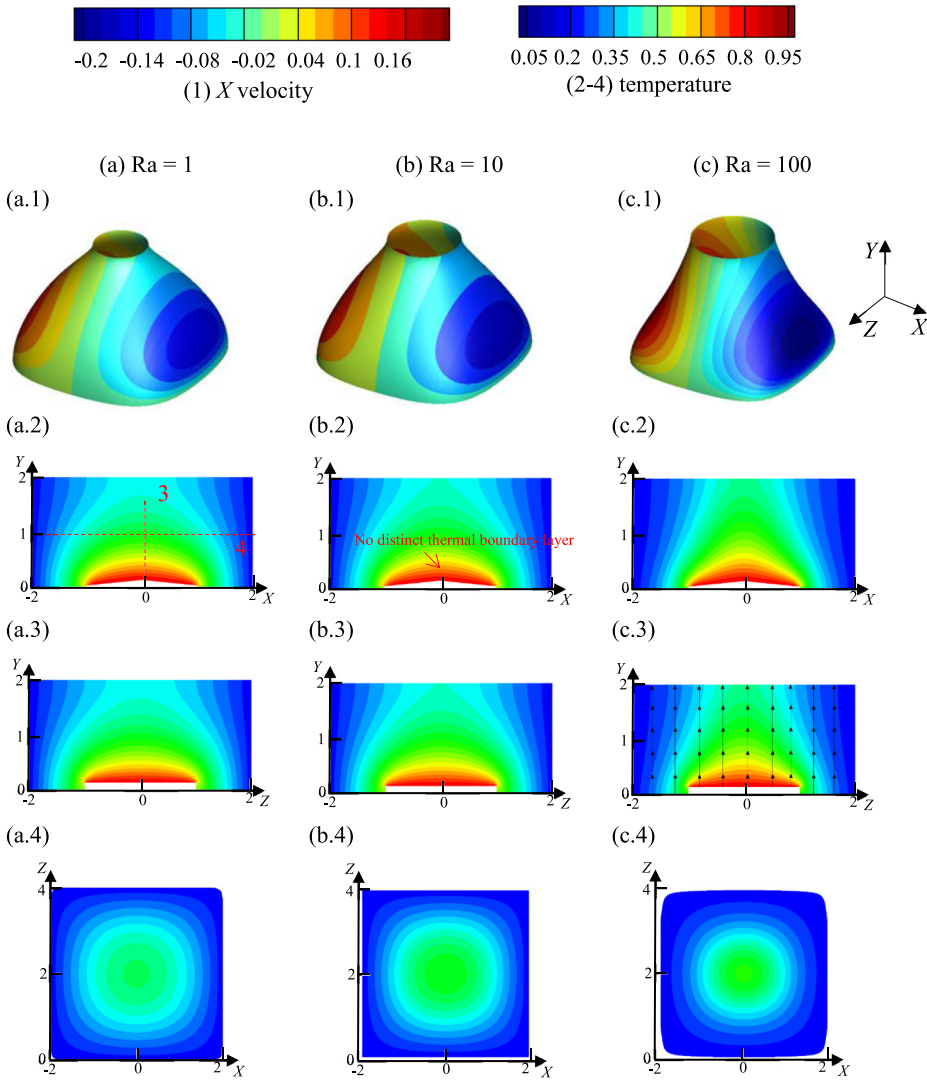
FIG. 3. Conduction-dominant weak flow and temperature for (a) Ra = 1, (b) Ra = 10, and (c) Ra = 10^2, plotted for (1) X-velocity contour on $\theta = 0.2$ isothermal surface, and temperature contours on the planes (2) $Z = 2$, (3) $X = 0$, and (4) $Y = 1$.

regarded as the fourfold torus in the Y-Z plane. In this topological method, three values E, H and P are considered, which represent the number of elliptic, hyperbolic, and parabolic points, respectively [73]. For the open boundary condition in this study, no elliptic point can be observed in the computing domain. In fact, the streamlines are parallel to each other in the $X = 0$ plane in Fig. 3(c. 3), and $H = 1$ (the brown solid circle) occurs in Fig. 4(a. 3), which represents two different flow scenarios. Therefore, the results prove the existence of a primary bifurcation between Ra = 10^2 and Ra = 10^3. The transition from the conduction-dominant to the convection-dominant flow triggers the primary bifurcation for different types of flow structures. Secondary bifurcation takes place between Ra = 10^3 and 10^4, $P = 2$ in Fig. 4(c. 3), which leads to the separation of the plume. Further investigation shows that the development of the primary bifurcation does not affect
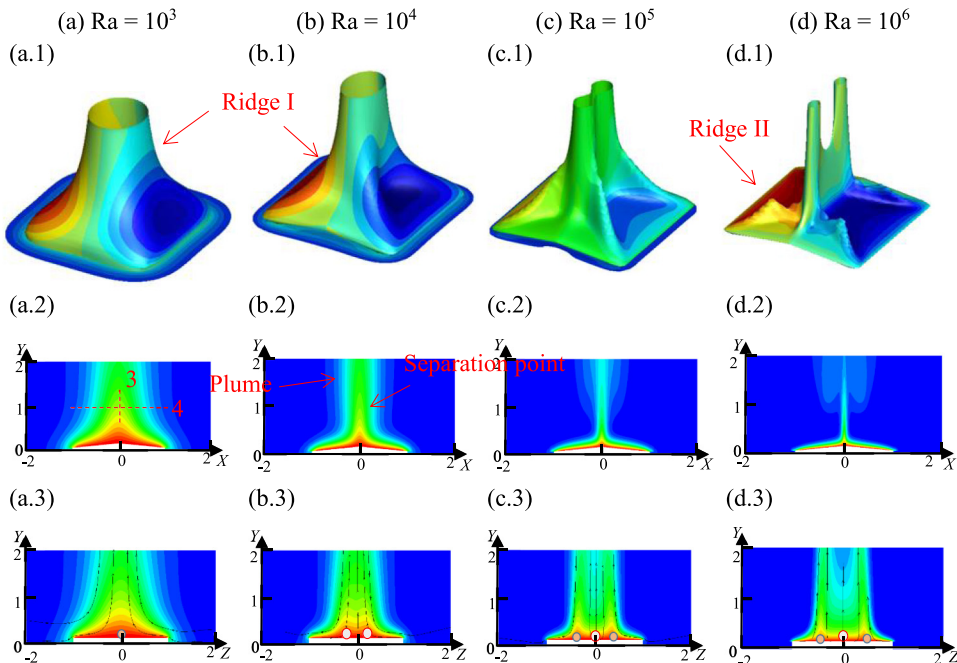
FIG. 4. Flow and temperature after the transition to a convection-dominant regime. Contours for(a) Ra = 10^3, (b) 10^4, (c) 10^5, and (d) 10^6 are plotted for (1) X velocity on $\theta = 0.2$ isothermal surface, (2) temperature on $Z = 2$ plane, (3) temperature on $X = 0$ plane with streamlines.

the flow regime. For Ra = 10^5, $H = 2$, $P = 1$ is clearly present in the $X = 0$ plane, which indicates that the tertiary bifurcation occurs between Ra = 10^4 and 10^5.

The flow structures influenced by leading edge effect is also shown in Fig. 5, where the streamlines on the plane situated $h = 0.01$ from the heated surface are plotted. For Ra = 10^3 [Fig. 5(a)], all streamlines converge near the center of the inclined heated plate, forming a plume downstream. For Ra = 10^4 [Fig. 5(b)], most streamlines tend to merge on a principal diagonal streamline, causing the occurrence of ridges (type of Ridge I in Fig. 4) near the edge of the inclined plate, while more streamlines are parallel in the center zone. As Ra is increased further, the ridges (type of Ridge II) act like an inclined plume stem, all streamlines near ridges gradually merge into the center stem and it results in the formation of one pair of plumes for Ra = 10^5 and 10^6 in Figs. 5(c) and 5(d) (also see Fig. 4). Based on the results in Ref. [50], different heating shapes may have different number of ridgelike structures rising from heated bottom area. However, in this study, the number of ridges is four since we are investigating a rectangular shape with the results in Ref. [50]. Furthermore, based on the literature [59], it is known that for a heated plate the ridges do not exist when the aspect ratio is large than 0.5.

C. Further pitchfork bifurcation: Transition within steady-state flows

Figure 6 shows the X velocity U_{Plume} at sampling point (0, 0.2, 1.5) in quasisteady state with increasing Ra. Here, the sampling point (0, 0.2, 1.5) was selected because different results at different points have the same bifurcation route as that at point (0, 0.2, 1.5) after a great number of numerical result examinations. Further, the quantity at the point (0, 0.2, 1.5), which is in the plume stem on the roof, may be used to characterize typical flows on the roof in the transition from steady to chaotic state. That is, U_{Plume} is the absolute X component of the velocity at the point inside the plume. When the flow is transitioning from conduction dominance to convection dominance, U_{Plume} could have a
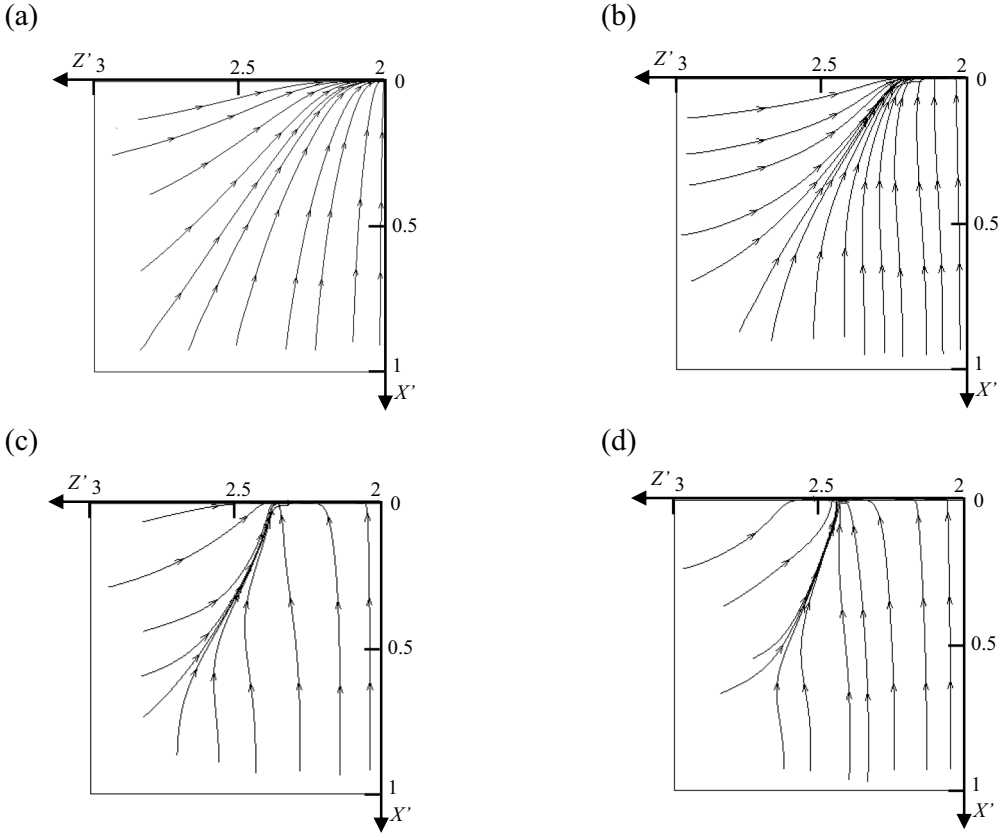
(a)

(b)

(c)

(d)

FIG. 5. Streamlines on quarter surface plane $(X' - Z')$ situated 0.01 from the heated plate for (a) Ra $= 10^3$, (b) Ra $=$ Ra $= 10^4$, (c) Ra $= 10^5$, and (d) Ra $= 10^6$.
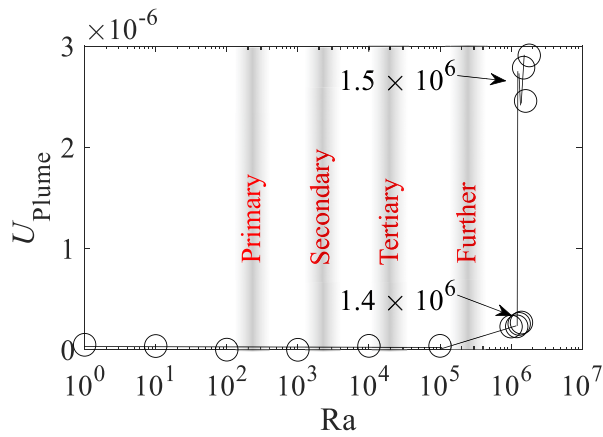
FIG. 6. Velocity in the X direction at point $(0, 0.2, 1.5)$ on plane $X = 0$. The shaded regions indicate the Ra ranges where pitchfork bifurcations occurred, based on the topological method.
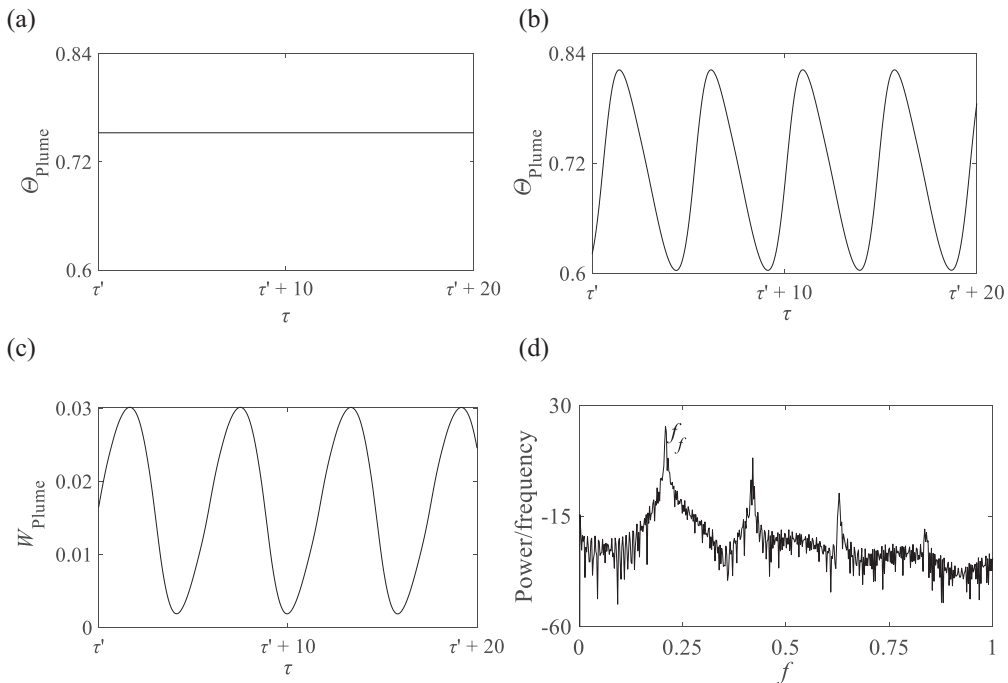
FIG. 7. Temperature history at point (0, 0.2, 1.5) for (a) $Ra = 1.9 \times 10^6$ and (b) 2×10^6. Z velocity at point (0, 0.2, 1.5) for (c) $Ra = 2 \times 10^6$. The corresponding power spectral density for (b) is plotted in (d), where $f_f = 0.209$.

significant increase. For $Ra < 10^5$, U_{Plume} is very close to zero, which means that the convective flow is very weak in the X direction. In the range of $10^5 < Ra < 1.4 \times 10^6$, a slight increment of U_{Plume} is observed. Then, U_{Plume} drastically increases in the range $1.4 \times 10^6 < Ra < 1.5 \times 10^6$, after which the flow loses the increase trend, so that another pitchfork bifurcation is expected between the computed flows. Except for the further pitchfork bifurcation, the other bifurcations described in Sec. III B based on the topology method are also plotted in Fig. 6. The ranges expected to occur are indicated by the shaded regions in Fig. 6.

D. Hopf bifurcation: Transition to periodic flows

Figure 7 plots the time series and its power spectral of the temperature and velocity probed at point (0, 0.2, 1.5). The time series used in Secs. III D–III G start from the time after the flow reaches the attractors (details about attractors at each Ra number can be seen in Fig. 15). Clearly, the temperature is constant for $Ra = 1.9 \times 10^6$ after it enters to a fully developed stage with the increase of time in Fig. 7(a) but becomes periodic for $Ra = 2 \times 10^6$ in Fig. 7(b). Since there is a flow transition from a steady state to a periodic state, a Hopf bifurcation exists between $Ra = 1.9 \times 10^6$ and 2×10^6. It is worth noting that when the flow slightly fluctuates with time, as shown in Fig. 7(c), the fundamental frequency of the flow is $f_f = 0.209$ with harmonic modes, as shown in Fig. 7(d). That is, the flow is periodic.

Flow structures and temperature profiles at three consecutive time intervals are plotted in Fig. 8. With the increase of Ra, the thermal boundary layer thickness decreases and the bulge is clearly observed in Figs. 8(a–c. 2). These bulges are produced by the stronger buoyant flows rising from edges of the surface and finally merging at the central stem of the plume. After the Hopf bifurcation, the plume stem fluctuates periodically with time, as shown by the contours in Fig. 8. In Figs. 8(a–c.
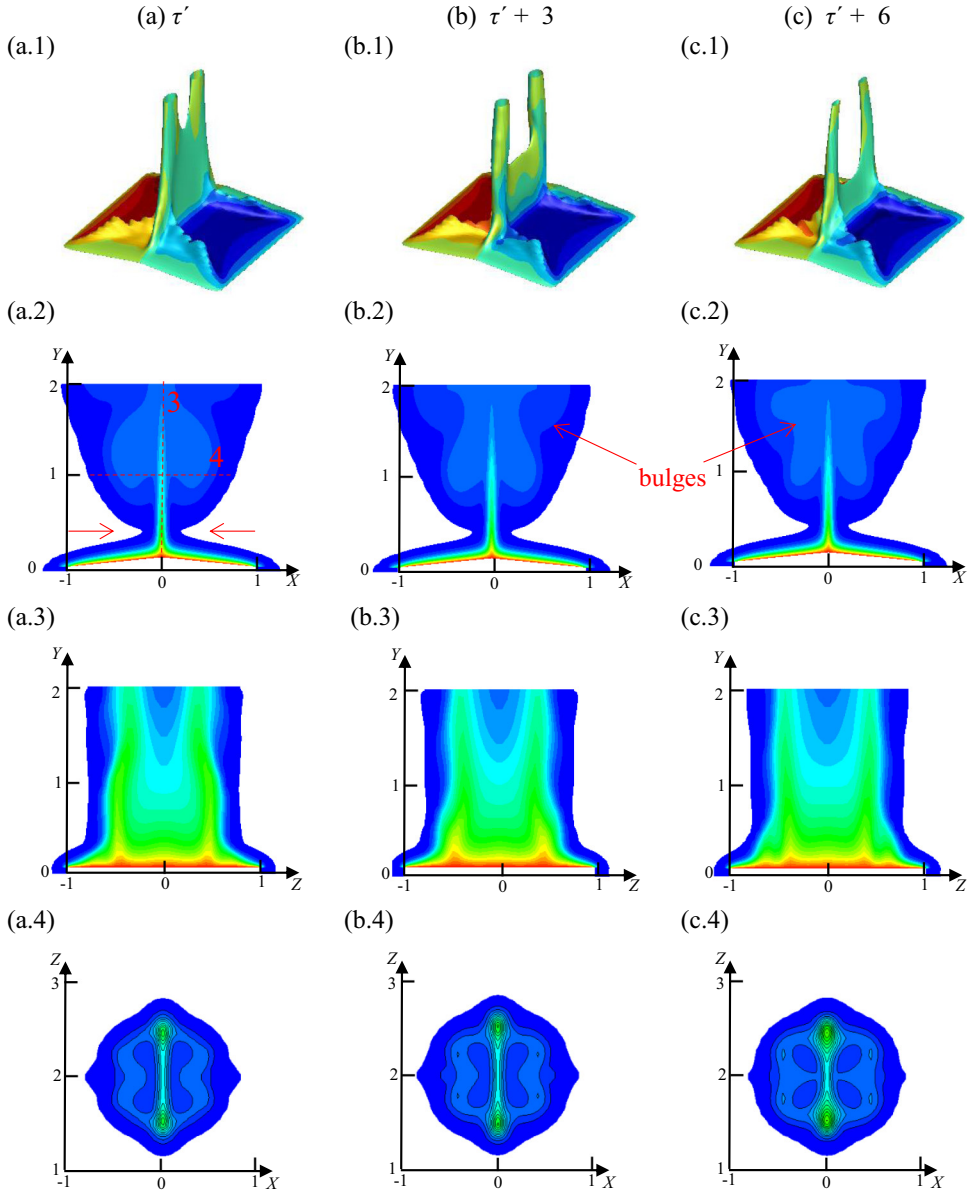
FIG. 8. Flow and temperature contours at Ra $= 2 \times 10^6$ after the onset of a Hopf bifurcation. Contours at (a) τ', (b) $\tau' + 3$, (c) $\tau' + 6$ are plotted for (1) X velocity on $\theta = 0.2$ isothermal surface, and temperature contours on the planes (2) $Z = 2$, (3) $X = 0$, and (4) $Y = 1$.

2), temperature contours at $Z = 2$ clearly show how the bulges occur near the top edge of the heated surface and merge to influence the plume. Temperature profiles on the plane $Y = 1$ shown in Figs. 8(a–c. 4) indicate a periodic flow fluctuation where the distance between convection rolls oscillates. In fact, although unsteady velocities in X or Z direction shown in Fig. 7(c) indicate that the flow is oscillatory, the oscillations are too small to identify only based on flow and temperature structures shown in Fig. 8. However, the further examination of numerical results shows that these small oscillations become larger with the increase of Ra.
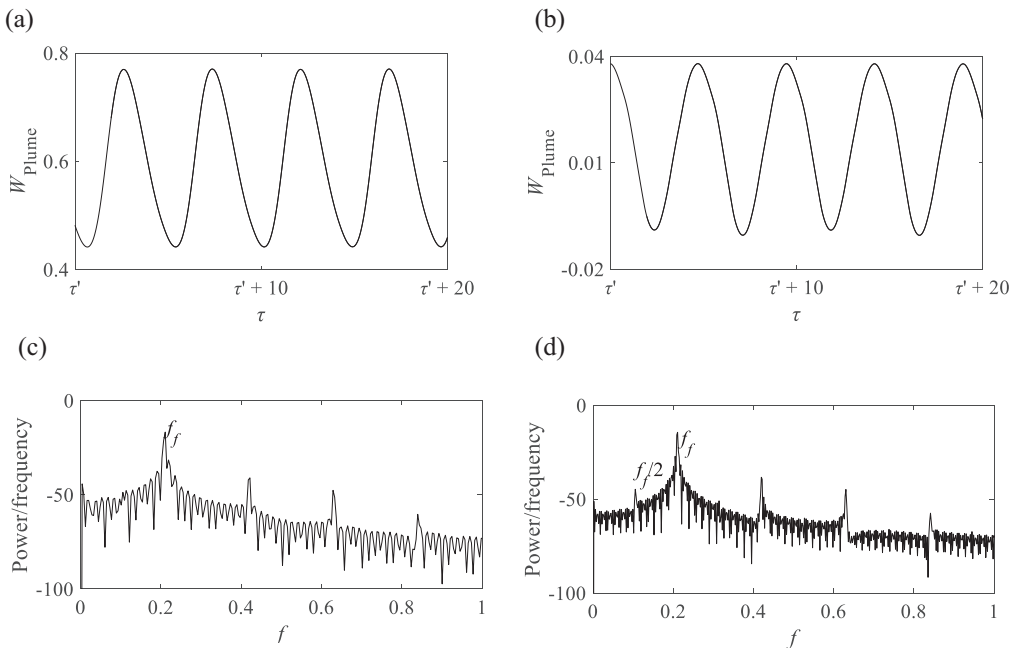
FIG. 9. Z velocity at point $(0, 0.2, 1.5)$ for (a) $\text{Ra} = 2.9 \times 10^6$, and (b) $\text{Ra} = 3 \times 10^6$, with corresponding power spectral densities in (c) and (d).

E. Period-doubling bifurcation

Figure 9 shows the velocity at point $(0, 0.2, 1.5)$ in the plume and corresponding power spectral density for $\text{Ra} = 2.9 \times 10^6$ and 3×10^6. Clearly, with the increase of Ra, the amplitude of Z velocity slightly increases. Additionally, there is a characteristic frequency of $f_f/2 = 0.105$ in the power spectral density for $\text{Ra} = 3 \times 10^6$ in Fig. 9(d), in comparison with that for $\text{Ra} = 2.9 \times 10^6$ in Fig. 9(c). This implies that a period doubling bifurcation occurs between $\text{Ra} = 2.9 \times 10^6$ and 3×10^6.

Figure 10 plots the flow structure after the onset of period-doubling bifurcation. The flow structure after the period-doubling bifurcation still remains approximately symmetric with respect to the plane $X = 0$, but with a stronger convective flow, as depicted in Figs. 10(a–c. 1). As shown in Figs. 10(a–c. 2), it is hard to observe the asymmetric structure with respect to $X = 0$ owing to the weak convection in the X direction. Additionally, a couple of bulges merge gradually with the stem in Fig. 10(a–c. 1), and then form a mushroom-shaped flow structure in Figs. 10(a–c. 2). Further, the separation of the stem in the YZ plane can also be seen in Figs. 10(a–c. 3). Figures 10(a–c. 4) show that strong convection occurs within a cycle with flow patterns still symmetric with respect to $X = 0$. However, in contrast to Figs. 8(a–c. 4), the plume becomes narrower and finally separates into two single plumes. This means that convection influences the stem of the plume, which could potentially lead to a break of symmetry.

F. Quasiperiodic bifurcation

Figure 11 plots the Z velocity and power spectral density of the near-field plume for $\text{Ra} = 3.4 \times 10^6$ and 3.5×10^6. Periodic motion is shown in Figs. 11(a) and 11(b). Further, an additional frequency f_{f2} is found and marked in Fig. 11(d) compared with Fig. 11(c). It is clear that f_f and f_{f2} have no multiple relationship, $f_q = f_f - f_{f2}$. This means that a quasiperiodic bifurcation occurs at 3.5×10^6 (see Zhao et al. [75] for details of quasiperiodic bifurcation). To further investigate
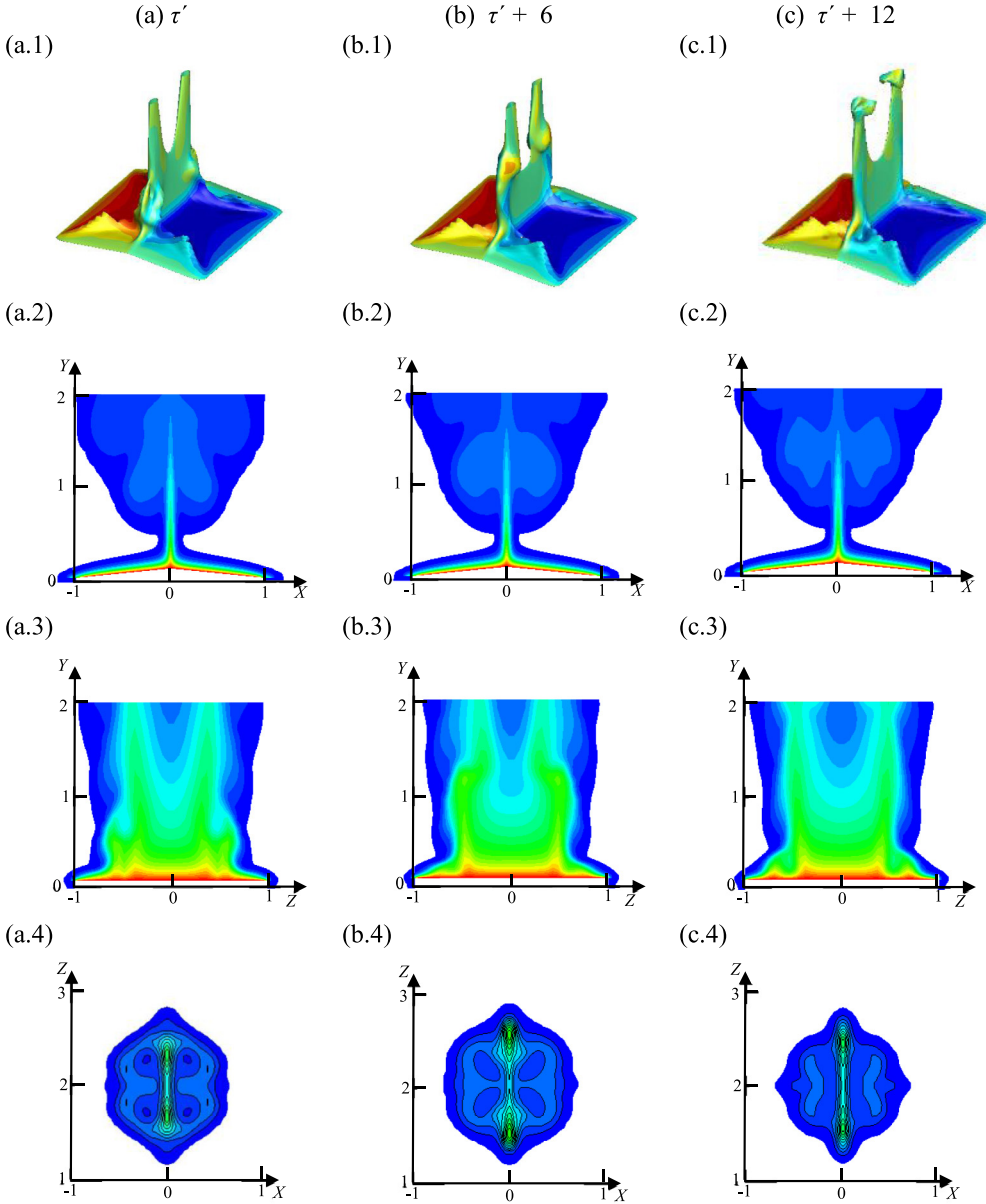
FIG. 10. Flow and temperature for Ra $= 3 \times 10^6$ after onset of period-doubling bifurcation. Contours at (a) τ', (b) $\tau' + 6$, (c) $\tau' + 12$ are plotted for (1) X velocity on $\theta = 0.2$ isothermal surface, and temperature on the orthogonal planes of (2) $Z = 2$, (3) $X = 0$, and (4) $Y = 1$.

the quasiperiodic bifurcation, some harmonic frequencies are found, as depicted in Fig. 11(d), which have a linear relationship with f_f and f_{f2} where $f_2 = f_f + f_{f_2}$, together with subharmonic frequency $f_{f2}/2$.

G. Chaotic flow

The examination of numerical results shows that the flow may be chaotic for sufficiently large values of Ra. Figure 12 plots the temperature in the plume for Ra $= 3.7 \times 10^6$ and 5×10^6. Clearly,
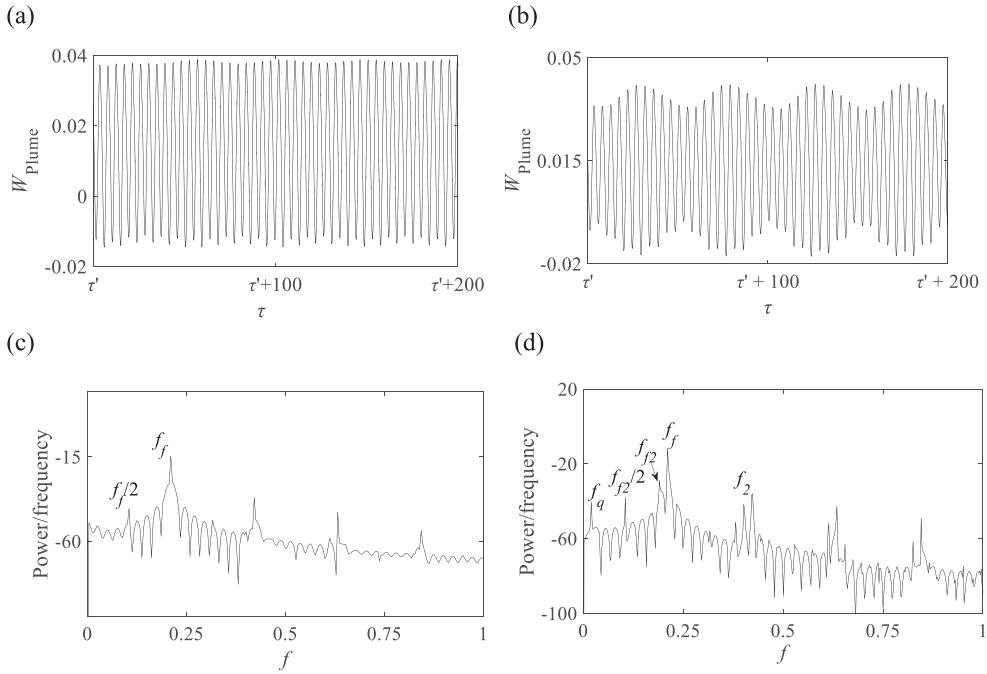
(a)

(b)

(c)

(d)

FIG. 11. Z velocity at point (0, 0.2, 1.5) for (a) Ra = 3.4×10^6 and (b) Ra = 3.5×10^6 with respective power spectral densities in (c) and (d).
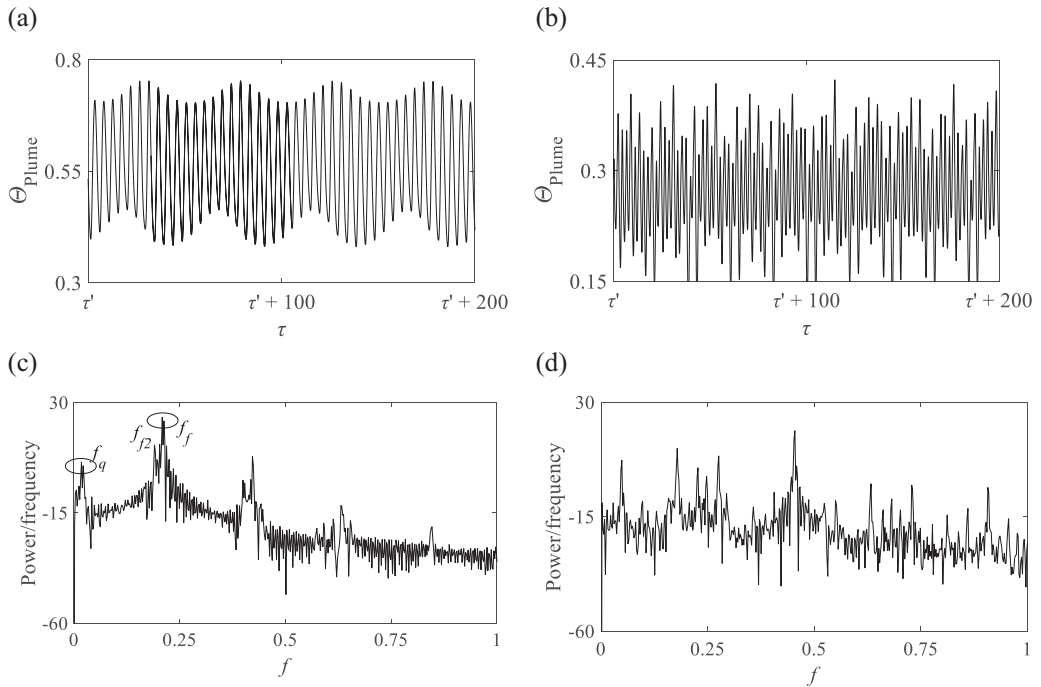
(a)

(b)

(c)

(d)

FIG. 12. Temperature evolution at point (0, 0.2, 1.5) for (a) Ra = 3.7×10^6 and (b) Ra = 5×10^6 with corresponding power spectral densities in (c) and (d).
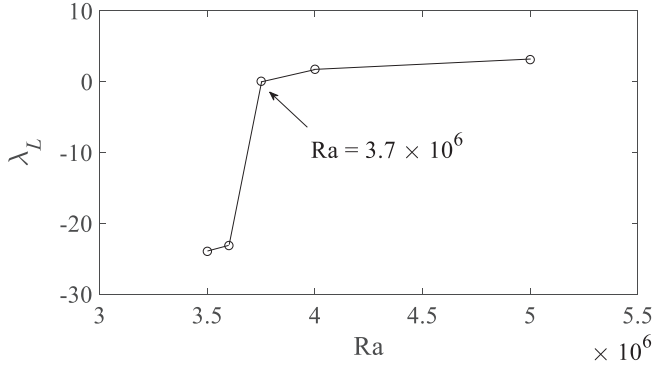
FIG. 13. The maximum Lyapunov exponent λ_L for different Rayleigh numbers.

the perfectly periodic flow is not present for Ra $= 3.7 \times 10^6$, as shown in Fig. 12(a). Additionally, the peak frequency of power spectral density becomes also bumpy, as shown in Fig. 12(c) for which there are still characteristic frequencies f_f, f_{f2} and f_q, corresponding to those in Figs. 12(c) and 12(d). This is because when the value of Ra is near the point of entering chaos, the flow still has dual properties of both periodic and chaotic flows (also see Li *et al.* [76]). Further increasing Ra to 5×10^6, the temperature becomes completely chaotic and power spectral density becomes flat without distinct peak frequency. That is, the periodic flow has ceased to exist.

To identify chaos, the maximum Lyapunov exponent (λ_L) is calculated. The definition of λ_L is referred by Odavic *et al.* [77] as

$$\lambda_L = \frac{1}{\tau_n - \tau_0} \sum_{i=1}^{n} \ln \frac{d_1(\tau_i)}{d_0(\tau_i)}. \tag{9}$$

In this equation, the two points P1 and P2 were selected in the orbit with an initial distance d_0. When the time of Δt has elapsed (e.g., 100 time steps), P1 and P2 arrived at new positions P1(τ_1) and P2(τ_1), and thus the distance between P1(τ_1) and P2(τ_1) becomes $d_1(\tau_1)$. Then we should find a new P'2(τ_1) to make the distance between P1(τ_1) and P'2(τ_1) ($d_0(\tau_1)$) approximately (limitation of time step and mesh grid) equal to d_0, then we start the next calculation. Elapsing another time of Δt, P1(τ_1) and P'2(τ_1) will arrive at new positions P1(τ_2) and P2(τ_2). Repeating this process for several times ($n > 50$), we obtained $d_0(\tau_1)$, $d_1(\tau_1)$, …, $d_0(\tau_n)$, $d_0(\tau_n)$. Details can be found in Ref. [77]. The orbit starts on the attractor (shown in Fig. 15) and Fig. 13 shows λ_L as a function of Ra. It is found that λ_L is positive if Ra is equal to or larger than 3.7×10^6, suggesting that the flow becomes chaotic in the range between 3.6×10^6 and 3.7×10^6.

Fractal dimension was also calculated to identify the bifurcations and chaos. The fractal dimension d_c can be given by

$$d_c = \lim_{s \to 0} \frac{\log(C_p(s))}{\log(s)}, \tag{10}$$

$$C_p(s) = \lim_{N \to 0} \frac{1}{N^2} \sum_{\substack{i,\,j=1 \\ i \neq j}}^{N} h(s - |\overrightarrow{X_i} - \overrightarrow{X_j}|), \tag{11}$$

where h is the Heaviside function, X_i and X_j are the values of data points (we selected the points in Fig. 15 as data points), N is the total number of data points, and s is the maximum distance between X_i and X_j. A detailed description can be found in Ref. [76]. It is known that a Hopf bifurcation can occur when d_c is close to 1, a quasiperiodic flow can appear when d_c is between 1 and 2, and

TABLE IV. Fractal dimension values for different Rayleigh numbers.

No.	Ra	Flow behavior	d_c
1	2×10^6	Periodic	0.9076
2	3.4×10^6	Quasiperiodic	1.591
3	3.7×10^6	Enter chaos	2.142
4	5×10^6	Chaos	2.116

the flow can enter into chaos when d_c is larger than 2. Table IV shows the calculation results for near-critical Ra, indicating that the flow behavior after each bifurcation.

To have a better understanding of the chaotic behavior, flow patterns are plotted with time for $Ra = 4 \times 10^6$. Figures 14(a–d. 1) confirm that the previously encountered symmetric structures with respect to the $X = 0$ and $Z = 2$ plane have broken. The temperature contours in the $Z = 2$ plane in Figs. 14(a–d. 2) reveal that the plume stem is fluctuating about $X = 0$ and the symmetric mushroom-shape flow structure has disappeared. Additionally, a couple of plume stems are still distinct with additional plumes rising from the top of the heated surface, as shown in Figs. 14(a–d. 3) in which additional plumes first merge with the main stem and then break the symmetric structure.
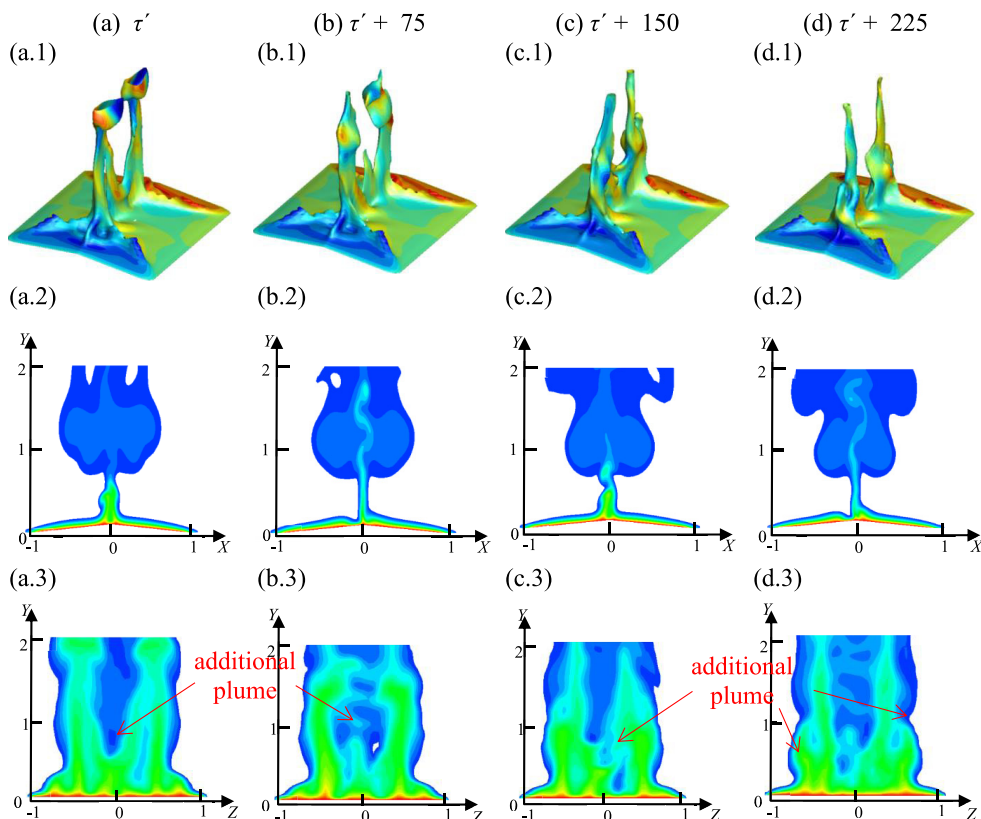

FIG. 14. Flow and temperature profiles for $Ra = 4 \times 10^6$. Contours at (a) τ', (b) $\tau' + 75$, (c) $\tau' + 150$, (d) $\tau' + 225$ are plotted for (1) X velocity on $\theta = 0.2$ isothermal surface, temperatures on the planes (2) $Z = 2$, (3) $X = 0$.
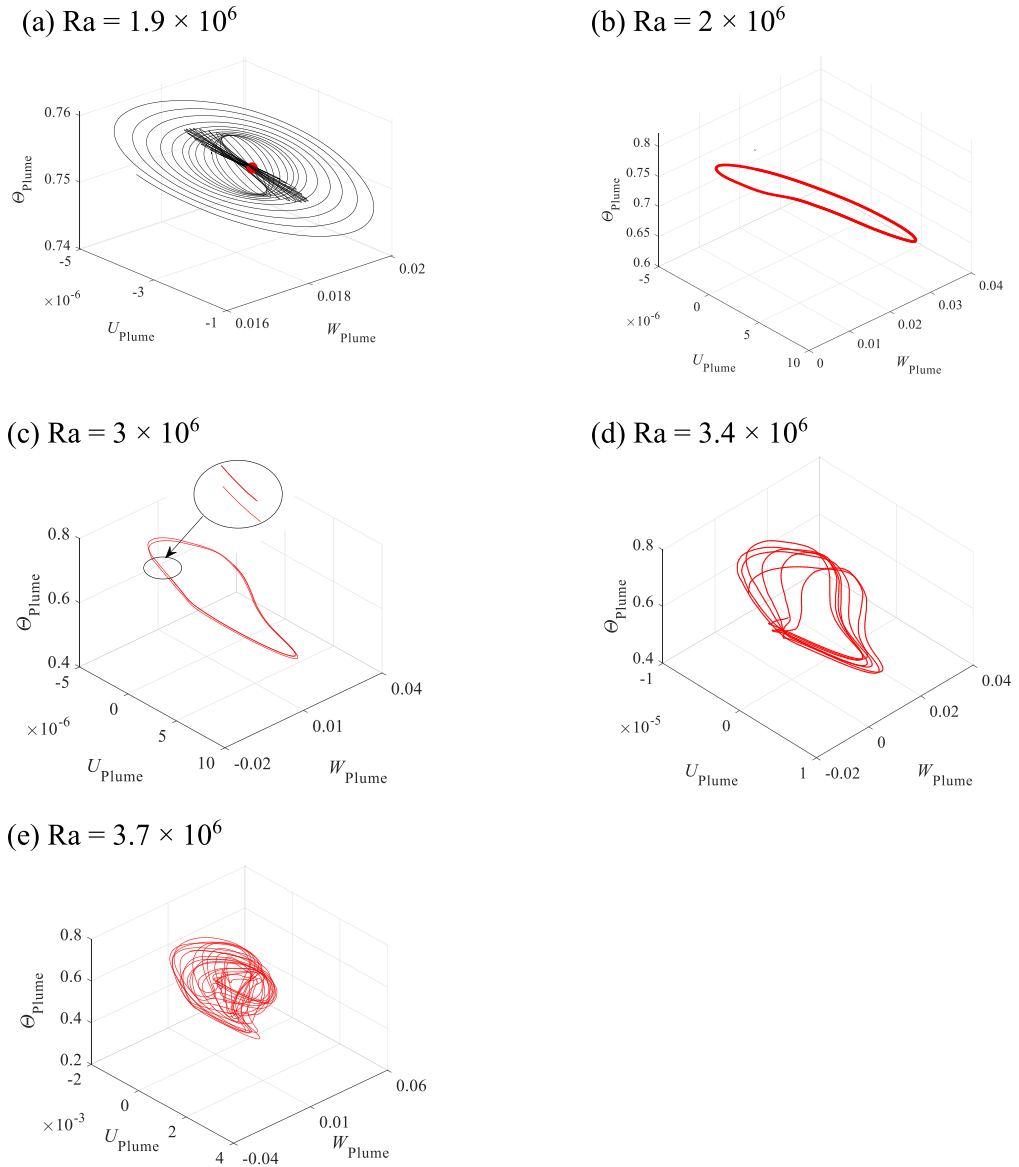
(a) Ra = 1.9×10^6

(b) Ra = 2×10^6

(c) Ra = 3×10^6

(d) Ra = 3.4×10^6

(e) Ra = 3.7×10^6

FIG. 15. Portrait of the X and Z velocities and temperature at point (0, 0.2, 1.5) as Ra is increased, showing the transitions of flow regime from laminar to chaos.

To better understand the route from laminar to chaos, trajectories of flows in their state space are plotted in Fig. 15 for different flow regimes. All results are in the fully developed stage in order to consider the dynamic in the plume. First, after the primary bifurcation, the flow in the fully developed stage is steady and the trajectory of velocity in different directions eventually approaches the fixed points indicated in Fig. 15(a) for Ra = 1.9×10^6, but it changes to a limit cycle after the Hopf bifurcation when Ra increases to 2×10^6 in Fig. 15(b), corresponding to a periodic flow. Further increasing Ra results in an increase of convection in the Z direction and a period-doubling bifurcation occurs with the appearance of the half fundamental frequency. Therefore, a double
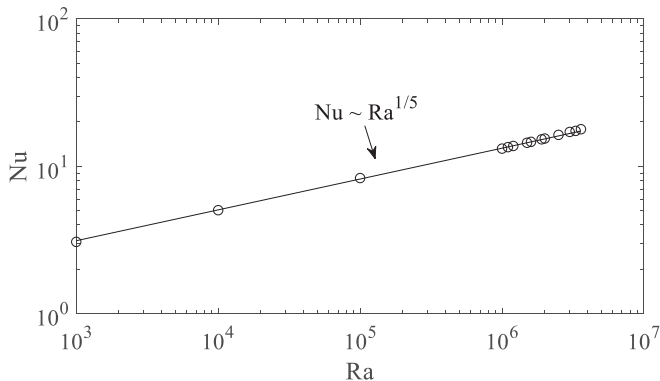
FIG. 16. Nusselt number of the flow over the inclined plate as a function of Ra.

toruslike curve forms in the state space for $Ra = 3 \times 10^6$, as shown in Fig. 15(c) and zoom. The convective flow in the Z direction becomes much stronger by increasing Ra. In the meantime, the flow structure is fluctuating to each side. As shown in Fig. 15(d), multiple circling tori swirl around a fixed axis for $Ra = 3.4 \times 10^6$. With the increase of Ra, the further quasiperiodic bifurcation occurs, and the flow finally reaches a chaotic state for $Ra = 3.7 \times 10^6$ in Fig. 15(e), which is consistent with the results shown in Fig. 13 and Table IV.

To investigate the influence of bifurcations on heat transfer, the Nusselt number, Nu, on the surface of the roof is calculated. The relationship of Nu as a function of Ra is plotted in Fig. 16, demonstrating that Nu is scaled by $Ra^{1/5}$ before the flow transition to chaos, which means that the bifurcation stage will not significantly influence the heat transfer. The result reveals that the relationship between Nu and Ra in a triangular isothermal structure is similar with the results in the horizontal or slightly inclined plate [21].

IV. CONCLUSIONS

An investigation on a buoyant plume emerging from an isothermal 3D surface on a section-triangular roof was presented using DNS. A large range of Ra from 1 to 5×10^6 is considered for the flow at a fixed Pr of 0.71, covering the flow from steady-state laminar to chaos, focusing on its transition. Flow structures and dynamics in different scenarios are provided and heat transfer was analyzed. Topological analysis was also used to better understand the symmetry breaking after a set of bifurcations.

In the route from the laminar to the chaos of the flow, when the Ra is relatively low ($Ra < 10^3$), the flow is under a conduction-dominant regime with symmetric flow structure in the steady state. With the increase of Ra, a first primary bifurcation occurs around $Ra = 10^2$ to 10^3 based on the topological analysis, resulting in a distinct plume stem. A secondary bifurcation then occurs around $Ra = 10^3$ to 10^4, which is characterized by four rising bulges. While the stem of the plume is divided into two parts with the flow gradually dominated by convection, a tertiary bifurcation takes place around $Ra = 10^4$ to 10^5. When Ra increases to 1.5×10^6, a further pitchfork bifurcation is seen and the stem separates. Further increasing Ra, a Hopf bifurcation occurs in the slope flow around $Ra = 2 \times 10^6$, in which the flow becomes periodic and a limit circle is observed in the state space, with a fundamental frequency f_f. Following that, the period-doubling bifurcation occurs when Ra increases from 2.9×10^6 to 3×10^6, forming a double toruslike curve in the limit cycle space. After Ra reaches 3.4×10^6, quasiperiod bifurcation appears in the slope flow, resulting in an additional frequency component. Finally, a chaotic state of the flow was confirmed at $Ra = 3.7 \times 10^6$, in which the bulge motion breaks the structure of the plume.

This study characterizes the route from laminar to chaos of the buoyant plume on the surface of a section-triangular roof with a fixed aspect ratio and Prandtl number. It is worth noting that the route from laminar to chaos might vary based on different geometry and Prandtl number, e.g., Li *et al.* [76]. The dynamics of the plume on the roof-shaped surface changes with increasing Ra. The effect of the aspect ratio on the critical Ra for primary, secondary, and tertiary pitchfork bifurcations is yet to be clarified, together with the dynamics and heat transfer characteristics for different Prandtl numbers, both of which motivate future work.

[1] R. P. Dring and B. Gebhart, A theoretical investigation of disturbance amplification in external laminar natural convection, J. Fluid Mech. **34**, 551 (1968).

[2] B. Nie and F. Xu, Scales of natural convection on a convectively heated vertical wall, Phys. Fluids **31**, 024107 (2019).

[3] Y. Zhao, P. Zhao, Y. Liu, Y. Xu, and J. F. Torres, On the selection of perturbations for thermal boundary layer control, Phys. Fluids **31**, 104102 (2019).

[4] B. Soderholm, B. Ronalds, and D. J. Kirshbaum, The evolution of convective storms initiated by an isolated mountain ridge, Mon. Weather Rev. **142**, 1430 (2014).

[5] G. T. Atkinson, D. D. Drysdale, and Y. Wu, Fire driven flow in an inclined trench, Fire Saf. J. **25**, 141 (1995).

[6] E. Fedorovich and A. Shapiro, Structure of numerically simulated katabatic and anabatic flows along steep slopes, Acta Geophys. **57**, 981 (2009).

[7] Y. Fan, Y. Li, J. Hang, K. Wang, and X. Yang, Natural convection flows along a 16-story high-rise building, Build. Environ. **107**, 215 (2016).

[8] H. F. Oztop, Y. Varol, and A. Koca, Laminar natural convection heat transfer in a shed roof with or without eave for summer season, Appl. Therm. Eng. **27**, 2252 (2007).

[9] L. Shi, G. Zhang, X. Cheng, Y. Guo, J. Wang, and M. Y. L. Chew, Developing an empirical model for roof solar chimney based on experimental data from various test rigs, Build. Environ. **110**, 115 (2016).

[10] S. C. Saha and M. M. K. Khan, A review of natural convection and heat transfer in attic-shaped space, Energy Build. **43**, 2564 (2011).

[11] H. Gunerhan and A. Hepbasli, Determination of the optimum tilt angle of solar collectors for building applications, Build. Environ. **42**, 779 (2007).

[12] S. Jalal, T. Van De Moortele, O. Amili, and F. Coletti, Steady and oscillatory flow in the human bronchial tree, Phys. Rev. Fluids **5**, 063101 (2020).

[13] H. Zhai, F. Xu, S. C. Saha, and Y. Hou, Natural convection and heat transfer on a section-triangular roof, Int. Commun. Heat Mass Transf. **92**, 23 (2018).

[14] H. Zhai, B. Nie, B. Chen, and F. Xu, Unsteady flows on a roof imposed by a periodic heat flux: 2D simulation and scaling analysis, Int. J. Therm. Sci. **145**, 106002 (2019).

[15] L. Prandtl, Führer durch die Strömungslehre, *Führer Durch Die Strömungslehre* (1942).

[16] W. T. Kierkus, An analysis of laminar free convection flow and heat transfer about an inclined isothermal plate, Int. J. Heat Mass Transf. **11**, 241 (1968).

[17] B. R. Rich, An investigation of heat transfer from an inclined flat plate in free convection, Trans. Am. Soc. Mech. Eng. **75**, 489 (1953).

[18] T. Fujii and H. Imura, Natural-convection heat transfer from a plate with arbitrary inclination, Int. J. Heat Mass Transf. **15**, 755 (1972).

[19] T. Vogt, W. Ishimi, T. Yanagisawa, Y. Tasaka, A. Sakuraba, and S. Eckert, Transition between quasi-2D and 3D Rayleigh-Bénard convection in a horizontal magnetic field, Phys. Rev. Fluids **3**, 013503 (2018).

[20] X. Dong, S. Tian, and C. Liu, Correlation analysis on volume vorticity and vortex in late boundary layer transition, Phys. Fluids **30**, 014105 (2018).

[21] K. Komori, S. Kito, T. Nakamura, Y. Inaguma, and T. Inagaki, Fluid flow and heat transfer in the transition process of natural convection over an inclined plate, Heat Transf. - Asian Res. **30**, 648 (2001).

[22] S. C. Saha, J. C. Patterson, and C. Lei, Natural convection in attics subject to instantaneous and ramp cooling boundary conditions, Energy Build. **42**, 1192 (2010).

[23] S. C. Saha, J. C. Patterson, and C. Lei, Natural convection boundary-layer adjacent to an inclined flat plate subject to sudden and ramp heating, Int. J. Therm. Sci. **49**, 1600 (2010).

[24] S. C. Saha, J. C. Patterson, and C. Lei, Natural convection and heat transfer in attics subject to periodic thermal forcing, Int. J. Therm. Sci. **49**, 1899 (2010).

[25] S. C. Saha, J. C. Patterson, and C. Lei, Scaling of natural convection of an inclined flat plate: Ramp cooling condition, Int. J. Heat Mass Transf. **53**, 5156 (2010).

[26] D. J. Tritton, Transition to turbulence in the free convection boundary layers on an inclined heated plate, J. Fluid Mech. **16**, 417 (1963).

[27] L. Pera and B. Gebhart, Natural convection boundary layer flow over horizontal and slightly inclined surfaces, Int. J. Heat Mass Transf. **16**, 1131 (1973).

[28] B. S. M. Al-arabi, Natural convection heat transfer from inclined isothermal plates, Int. J. Heat Mass Transf. **31**, 559 (1988).

[29] E. M. Sparrow and R. B. Husar, Longitudinal vortices in natural convection flow on inclined plates, J. Fluid Mech. **37**, 251 (1969).

[30] J. R. Lloyd and E. M. Sparrow, On the instability of natural convection flow on inclined plates, J. Fluid Mech. **42**, 465 (1970).

[31] W. Z. Black and J. K. Norris, The thermal structure of free convection turbulence from inclined isothermal surfaces and its influence on heat transfer, Int. J. Heat Mass Transf. **18**, 43 (1975).

[32] F. Picella, J. C. Robinet, and S. Cherubini, On the influence of the modelling of superhydrophobic surfaces on laminar-turbulent transition, J. Fluid Mech. **901**, 15 (2020).

[33] A. S. Alzwayi, M. C. Paul, and S. Navarro-Martinez, Large eddy simulation of transition of free convection flow over an inclined upward facing heated plate, Int. Commun. Heat Mass Transf. **57**, 330 (2014).

[34] G. C. Vliet, Natural convection local heat transfer on constant-heat-flux inclined surfaces, J. Heat Transfer **91**, 511 (1969).

[35] M. C. Paul, D. A. S. Rees, and M. Wilson, The influence of higher order effects on the vortex instability of thermal boundary layer flow in a wedge-shaped domain, Int. J. Heat Mass Transf. **48**, 1417 (2005).

[36] D. Puigjaner, J. Herrero, F. Giralt, and C. Simó, Stability analysis of the flow in a cubical cavity heated from below, Phys. Fluids **16**, 3639 (2004).

[37] J. F. Torres, D. Henry, A. Komiya, S. Maruyama, and H. Ben Hadid, Three-dimensional continuation study of convection in a tilted rectangular enclosure, Phys. Rev. E **88**, 043015 (2013).

[38] J. F. Torres, D. Henry, A. Komiya, and S. Maruyama, Bifurcation analysis of steady natural convection in a tilted cubical cavity with adiabatic sidewalls, J. Fluid Mech. **756**, 650 (2014).

[39] J. F. Torres, D. Henry, A. Komiya, and S. Maruyama, Transition from multiplicity to singularity of steady natural convection in a tilted cubical enclosure, Phys. Rev. E **92**, 023031 (2015).

[40] C. M. Hocut, D. Liberzon, and H. J. S. Fernando, Separation of upslope flow over a uniform slope, J. Fluid Mech. **775**, 266 (2015).

[41] F. Kimura, T. Yoshioka, K. Kitamura, M. Yamaguchi, and T. Asami, Fluid flow and heat transfer of natural convection at a slightly inclined, upward-facing, heated plate, Heat Transf. - Asian Res. **31**, 362 (2002).

[42] J. T. BR Morton and G Taylor, Turbulent gravitational convection from maintained and instantaneous, Proc. R. Soc. London Ser. A **234**, 125 (1956).

[43] A. Koca, H. F. Oztop, and Y. Varol, The effects of prandtl number on natural convection in triangular enclosures with localized heating from below, Int. Commun. Heat Mass Transf. **34**, 511 (2007).

[44] X. Xu, G. Sun, Z. Yu, Y. Hu, L. Fan, and K. Cen, Numerical investigation of laminar natural convective heat transfer from a horizontal triangular cylinder to its concentric cylindrical enclosure, Int. J. Heat Mass Transf. **52**, 3176 (2009).

[45] T. K. Fanneløp and D. M. Webber, On buoyant plumes rising from area sources in a calm environment, J. Fluid Mech. **497**, 319 (2003).

[46] D. B. Spalding and R. G. Cruddace, Theory of the steady laminar buoyant flow above a line heat source in a fluid of large prandtl number and temperature-dependent viscosity, Int. J. Heat Mass Transf. **3**, 55 (1961).

[47] K. E. Torrance, L. Orloff, and J. A. Rockett, Experiments on natural convection in enclosures with localized heating from below, J. Fluid Mech. **36**, 21 (1969).

[48] X. Jiang and K. H. Luo, Direct numerical simulation of the near field dynamics of a rectangular reactive plume, Int. J. Heat Fluid Flow **22**, 633 (2001).

[49] A. Kondrashov, I. Sboev, and K. Rybkin, Effect of boundary conditions on thermal plume growth, Heat Mass Transf. **52**, 1359 (2016).

[50] A. Kondrashov, I. Sboev, and P. Dunaev, Evolution of convective plumes adjacent to localized heat sources of various shapes, Int. J. Heat Mass Transf. **103**, 298 (2016).

[51] A. Kondrashov and E. Burkova, Stationary convective regimes in a thin vertical layer under the local heating from below, Int. J. Heat Mass Transf. **118**, 58 (2018).

[52] T. Hattori, S. E. Norris, M. P. Kirkpatrick, and S. W. Armfield, Simulation and analysis of puffing instability in the near field of pure thermal planar plumes, Int. J. Therm. Sci. **69**, 1 (2013).

[53] T. Hattori, N. Bartos, S. E. Norris, M. P. Kirkpatrick, and S. W. Armfield, Experimental and numerical investigation of unsteady behaviour in the near-field of pure thermal planar plumes, Exp. Therm. Fluid Sci. **46**, 139 (2013).

[54] T. Hattori, S. E. Norris, M. P. Kirkpatrick, and S. W. Armfield, Prandtl number dependence and instability mechanism of the near-field flow in a planar thermal plume, J. Fluid Mech. **732**, 105 (2013).

[55] F. Plourde, M. V. Pham, S. D. Kim, and S. Balachandar, Direct numerical simulations of a rapidly expanding thermal plume: Structure and entrainment interaction, J. Fluid Mech. **604**, 99 (2008).

[56] M. Qiao, F. Xu, and S. C. Saha, Numerical study of the transition to chaos of a buoyant plume from a 2D open cavity heated from below, Appl. Math. Model. **61**, 577 (2018).

[57] M. Qiao, Z. F. Tian, B. Nie, and F. Xu, The route to chaos for plumes from a top-open cylinder heated from underneath, Phys. Fluids **30**, 124102 (2018).

[58] D. Das and T. Basak, Role of distributed/discrete solar heaters during natural convection in the square and triangular cavities: CFD and heatline simulations, Sol. Energy **135**, 130 (2016).

[59] S. Kenjereš, Heat transfer enhancement induced by wall inclination in turbulent thermal convection, Phys. Rev. E **92**, 053006 (2015).

[60] S. Bhowmick, S. C. Saha, M. Qiao, and F. Xu, Transition to a chaotic flow in a V-shaped triangular cavity heated from below, Int. J. Heat Mass Transf. **128**, 76 (2019).

[61] G. Launay, T. Cambonie, D. Henry, A. Pothérat, and V. Botton, Transition to chaos in an acoustically driven cavity flow, Phys. Rev. Fluids **4**, 044401 (2019).

[62] T. Adachi, Stability of natural convection in an inclined square duct with perfectly conducting side walls, Int. J. Heat Mass Transf. **49**, 2372 (2006).

[63] J. F. Torres, Y. Zhao, S. Xu, Z. Li, and A. Komiya, Optical method for simultaneous high-resolution measurement of heat and fluid flow: The case of Rayleigh-Bénard convection, Phys. Rev. Appl. **14**, 54038 (2020).

[64] D. Linton and B. Thornber, Direct numerical simulation of transitional flow in a staggered tube bundle, Phys. Fluids **28**, 024111 (2016).

[65] T. A. Smith and Y. Ventikos, Boundary layer transition over a foil using direct numerical simulation and large eddy simulation, Phys. Fluids **31**, 124102 (2019).

[66] S. K. W. Tou, C. P. Tso, and X. Zhang, 3-D numerical analysis of natural convective liquid cooling of a 3 x 3 heater array in rectangular enclosures, Int. J. Heat Mass Transf. **42**, 3231 (1999).

[67] S. V. Patankar, *Numerical heat transfer and fluid flow* (Hemisphere Publishing Corp., Washington, 1980).

[68] B. P. Leonard and S. Mokhtari, Ultra-sharp non-oscillatory convection schemes for high-speed steady multidimensional flow, NASA Tech. Memo. 1 (1990).

[69] ANSYS Fluent 12.0 theory guide.

[70] E. Zhou and Y. Bayazitoglu, Developing laminar natural convection of power law fluids in vertical open ended channel, Int. J. Heat Mass Transf. **128**, 354 (2019).

[71] X. Wang, F. Xu, and H. Zhai, An experimental study of a starting plume on a mountain, Int. Commun. Heat Mass Transf. **97**, 1 (2018).

[72] I. D. Di Piazza and M. Ciofalo, Low-Prandtl number natural convection in volumetrically heated rectangular enclosures: I. Slender cavity, AR = 4, Int. J. Heat Mass Transf. **43**, 3027 (2000).

[73] T. W. H. Sheu, H. P. Rani, T. C. Tan, and S. F. Tsai, Multiple states, topology and bifurcations of natural convection in a cubical cavity, Comput. Fluids **37**, 1011 (2008).

[74] G. Metcalfe and J. M. Ottino, Experimental and computational studies of mixing in complex stokes flows: The vortex mixing flow and multicellular cavity flows, J. Fluid Mech. **269**, 199 (1994).

[75] Y. Zhao, C. Lei, and J. C. Patterson, Natural transition in natural convection boundary layers, Int. Commun. Heat Mass Transf. **76**, 366 (2016).

[76] T. F. Li, Z. G. Su, K. Luo, and H. L. Yi, Transition to chaos in electro-thermo-convection of a dielectric liquid in a square cavity, Phys. Fluids **32**, 013106 (2020).

[77] J. Odavić, P. Mali, and J. Tekić, Farey sequence in the appearance of subharmonic Shapiro steps, Phys. Rev. E **91**, 052904 (2015).